separations

MDPI

Article

Optimizing Vertical Zone Refining for Ultra-High-Purity Tin: Numerical Simulations and Experimental Analyses

Yu Yao [1], Jiajun Wen [1], Qi He [2], Meizhen Wu [2,*], Lishi Chen [2], Yuxu Bao [2] and Hongxing Zheng [1,3,*]

[1] School of Materials Science and Engineering, Shanghai University, Shanghai 200444, China; yaoyu_1@shu.edu.cn (Y.Y.); qingsyfwjj@163.com (J.W.)
[2] Yunnan Tin New Material Company Limited, Kunming 650501, China; heart198406@163.com (Q.H.); chenlishi9192@163.com (L.C.); baoyuxu5634206@126.com (Y.B.)
[3] Shanghai Engineering Research Center for Integrated Circuits and Advanced Display Materials, Shanghai University, Shanghai 200444, China
* Correspondence: wumeizhen516476@163.com (M.W.); hxzheng@shu.edu.cn (H.Z.)

Abstract: This study investigates the application of the vertical zone refining process to produce ultra-high-purity tin. Computational fluid dynamics (CFD) simulations were conducted using an Sn-1 wt.%Bi binary alloy to assess the effects of two key parameters—heater temperature and pulling rate—on Bi impurity segregation. The simulations revealed a dynamic evolution in molten zone height, characterized by an initial rapid rise, followed by a gradual increase and ending with a sharp decline. Despite these fluctuations, the lower solid–liquid interface consistently remained slightly convex. After nine zone passes, impurities accumulated at the top of the sample, with dual vortices forming a rhombus- or gate-shaped negative segregation zone. The simulations demonstrated that lower heater temperatures and slower pulling rates enhanced impurity segregation efficiency. Based on these results, experiments were performed using 6N-grade tin as the starting material. Glow discharge mass spectrometry (GDMS) analysis showed that the effective partition coefficients (k_{eff}) for impurities such as Ag, Pb, Co, Al, Bi, Cu, Fe, and Ni were significantly less than 1, while As was slightly below but very close to 1, and Sb was above 1. Under optimal conditions—405 °C heater temperature and a pulling rate of 5 μm/s—over 60% of impurities were removed after nine zone passes, approaching 6N9-grade purity. These findings provide valuable insights into optimizing the vertical zone refining process and demonstrate its potential for achieving 7N-grade ultra-high-purity tin.

Keywords: high-purity tin; vertical zone refining; numerical simulation; partition coefficient

Citation: Yao, Y.; Wen, J.; He, Q.; Wu, M.; Chen, L.; Bao, Y.; Zheng, H. Optimizing Vertical Zone Refining for Ultra-High-Purity Tin: Numerical Simulations and Experimental Analyses. *Separations* **2024**, *11*, 273. https://doi.org/10.3390/separations11090273

Academic Editor: Guoquan Zhang

Received: 24 August 2024
Revised: 17 September 2024
Accepted: 18 September 2024
Published: 19 September 2024

1. Introduction

High-purity and ultra-high-purity tin is indispensable for various cutting-edge applications, such as metal sputtering targets and extreme ultraviolet (EUV) light source systems. In EUV lithography machines, for instance, generating EUV light involves bombarding liquid tin droplets with high-power CO_2 lasers, and the emitted light is subsequently reflected by a Mo/Si-coated mirror. However, minimizing impurity-induced plasma debris formation from the tin droplets is crucial to maintaining high mirror reflectivity, necessitating exceptional tin purity levels [1]. The primary purification techniques for high-purity tin production are vacuum distillation, electrolytic refining, and zone refining. Each of these methods offers unique advantages and challenges, depending on the specific purity requirements and production scales. This paper provides an overview of recent advancements in these techniques, with a particular focus on the efficacy of the vertical zone refining process for producing ultra-high-purity tin.

Firstly, vacuum distillation relies on the differences in boiling points and saturated vapor pressures of various impurity elements in molten tin. Precise control of distillation temperature and vacuum conditions enables selective volatilization and condensation of impurities, segregating them into the vapor or liquid phase [2]. As early as 1952, Price

documented the low vapor pressure of tin at temperatures up to 1000 °C, achieving the removal of volatile constituents from tin-rich alloys via vacuum distillation [3]. Recently, Jia et al. conducted small-scale industrial experiments on the vacuum distillation of Pb-Sn alloys, achieving a notable reduction in lead (Pb) content in refined tin to less than 0.01 wt.% [4]. Nan et al. investigated the vapor–liquid equilibria for Sn-Bi binary alloys under vacuum conditions, demonstrated effective removal of bismuth (Bi) from crude tin, with tin content in the liquid phase exceeding 99.99 wt.% at temperatures above 1300 K [5]. Pu et al. addressed inefficiencies in arsenic (As) removal by adopting vacuum distillation for crude tin purification, achieving significant impurity removal with notable tin recovery rates and arsenic removal efficiencies under specific conditions [6]. Additionally, You et al. optimized vacuum distillation conditions for Sn-Sb alloys, achieving a tin content of 98.77 wt.% in the liquid phase and an antimony content of 98.77 wt.% in the vapor phase under specific parameters [7]. Vacuum distillation is now widely recognized as a waste-free, efficient, and industrially viable method for purifying low-purity tin, with potential for future applications in higher-purity tin production.

Secondly, electrolytic refining leverages the differences in standard electrode potentials between tin and its impurities. Impurities with lower electrode potentials than tin accumulate at the anode, while those with higher potentials remain in the electrolyte, facilitating the separation and purification of tin [8]. Gana et al. demonstrated the feasibility of using an AISI-316 stainless steel mesh basket as an anode support, enabling extended electrolysis without frequent interruptions for removing passive films [9]. Kulcsar et al. explored the electrolytic refining of tin-based lead-free soldering waste materials in chloride solutions, achieving high-purity tin deposits that exceeded industry standards [10]. They further employed electrolytic refining in hydrochloric acid–tin chloride solutions, achieving a cathodic current efficiency of over 90% and a cathode deposit purity nearing 99.99 wt.% through precise control of electrolyte composition [11]. Electrolytic refining is currently the leading method for the industrial production of 5N-grade tin.

Furthermore, zone refining of tin involves the gradual transformation of molten tin into a solid state under controlled atmospheres or vacuum conditions. The effectiveness of this process is primarily governed by the effective partition coefficients (k_{eff}) of impurities, and purification efficiency is closely linked to key process parameters such as heating temperature and the relative moving rate between the heater and the molten tin. Compared to vacuum distillation and electrolytic refining, zone refining typically achieves higher purity levels in the final product [12]. Zhang et al. reported that most impurities in molten tin exhibited k_{eff} values less than 1, with the exception of antimony (Sb), which had a value slightly above 1. Under optimized conditions—using a heater movement rate of 0.6 mm/min and performing 10 zone passes—the purity of tin increased from 99.99682 wt.% to 99.99906 wt.% [13]. To further understand impurity segregation mechanisms, Lee et al. developed a model incorporating solute transport resistance in the melt, which accurately predicted the distribution of impurities such as Pb and Bi during zone refining. Their experimental results aligned well with the simulated data, enhancing the understanding of impurity behavior in the refining process [14]. Given the computational demands of traditional optimization methods like trial-and-error and numerical simulations, Cheung et al. introduced a machine learning genetic algorithm to optimize impurity distribution during zone refining. This predictive model allowed for determining optimal zone lengths in each pass, maximizing purification efficiency, minimizing material waste, and reducing the number of required zone passes [15].

From an engineering perspective, while horizontal zone refining is effective for producing 6N-grade high-purity tin, achieving higher grades often requires additional zone passes, which can lead to reduced yield and increased production costs. Specifically for low-melting metals, horizontal zone refining encounters limitations, such as difficulty in controlling the molten zone width and inadequate separation of impurities. These challenges can hinder its effectiveness in reaching ultra-high purity levels. In contrast, vertical zone refining offers significant advantages due to its more favorable thermal environment.

This process provides precise control over temperature gradients and the morphology of the solid–liquid interface, both of which are crucial for enhancing impurity segregation. Previous research has shown that vertical zone refining can significantly improve purity levels. For instance, studies have reported improvements from 6N-grade indium (99.999985 wt.%) to 7N-grade (99.999991 wt.%) [16,17], and from 5N-grade tin (99.99983 wt.%) to 6N4-grade purity (99.99994 wt.%) [18]. However, the challenge of achieving 7N-grade ultra-high-purity tin remains significant. The effectiveness of vertical zone refining at such high levels of purity is uncertain, particularly since the impurity segregation behaviors seen in lower-purity processes may not directly apply to ultra-high-purity materials. To address these challenges, this study combines computational fluid dynamics (CFD) simulations with experimental research. The CFD simulations were used to explore the effects of critical parameters—heater temperature and pulling rate—on impurity segregation using an Sn-1 wt.%Bi alloy as a model system. The insights gained from these simulations were then applied in experiments to optimize impurity separation, with the goal of evaluating the feasibility of producing ultra-high-purity tin through vertical zone refining.

2. Numerical Simulations and Experimental Procedure

In this study, the Sn-1 wt.%Bi alloy was selected as the model system. The key thermophysical parameters used in the numerical simulations are presented in Table 1 [19,20]. The experimental setup for vertical zone refining is shown in Figure 1a. To ensure computational accuracy, the vertical zone refining apparatus was simplified in design, and the geometry was modeled using quadrilateral mesh grids, as depicted in Figure 1b. The mesh distribution across various regions of the model was as follows: quartz tube (1604 cells), Sn-1 wt.%Bi alloy (3000 cells), tantalum wire (169 cells), annular boron nitride (1134 cells), mica plate (1270 cells), cooling trap system (5720 cells), insulation layer (9960 cells), argon gas within the vacuum chamber (90,282 cells), and stainless-steel guide rod (4894 cells).

Table 1. Thermophysical properties of Sn-1 wt.%Bi alloy [19,20].

Parameter	Symbol	Value	Unit
Solid density	ρ_0	7.298×10^3	kg/m^3
Specific heat	C_P	2.26×10^2	J/(kg·K)
Thermal conductivity	k	67	W/(m·K)
Viscosity	μ	1.593×10^{-3}	kg/(m·s)
Solute diffusivity in liquid phase	D_l	3×10^{-9}	m^2/s
Solute diffusivity in solid phase	D_s	1×10^{-12}	m^2/s
Thermal expansion coefficient	β_T	9.5×10^{-5}	/K
latent heat of melting	ΔH_f	2.88×10^4	J/kg
Solute expansion coefficient	β_c	3.8×10^{-3}	/(wt.%)
Solidus temperature	T_s	227.5	°C
Liquidus temperature	T_L	231.5	°C
Equilibrium partition coefficient	k_0	0.30	-

For the vertical zone refining experiments, 6N-grade tin was used as the starting material. The experimental procedure was as follows: A quartz tube containing approximately 100 g of tin was positioned at the initial location, with the bottom of the quartz tube aligned with the mica plate above the heater coil. After evacuating the system to a pressure of 1×10^{-4} Pa, argon was introduced to a pressure of 0.03 MPa. The heater was then activated, and the temperature was increased to the target level. The heater temperature was monitored using a K-type thermocouple, with feedback used to regulate the heating power. The temperature was controlled with an accuracy of ±0.1 °C. After maintaining the target temperature for 20 min, the first zone pass was performed at a specified pulling rate. The quartz tube was then returned to its initial position, and eight additional zone passes were carried out in a cyclic manner before extracting the sample. Samples were taken from the bottom, middle, and top of the refined material for composition analysis using Glow Discharge Mass Spectrometry (GDMS). Key experimental parameters included: the

top mica plate being 13 mm from the heater coil's horizontal centerline; the alloy sample dimensions of 12 mm (diameter) × 120 mm (height); the quartz tube dimensions of 15 mm (outer diameter) × 160 mm (height); the inner diameter of the annular boron nitride being 20 mm; and the cooling trap inner diameter being 23 mm.

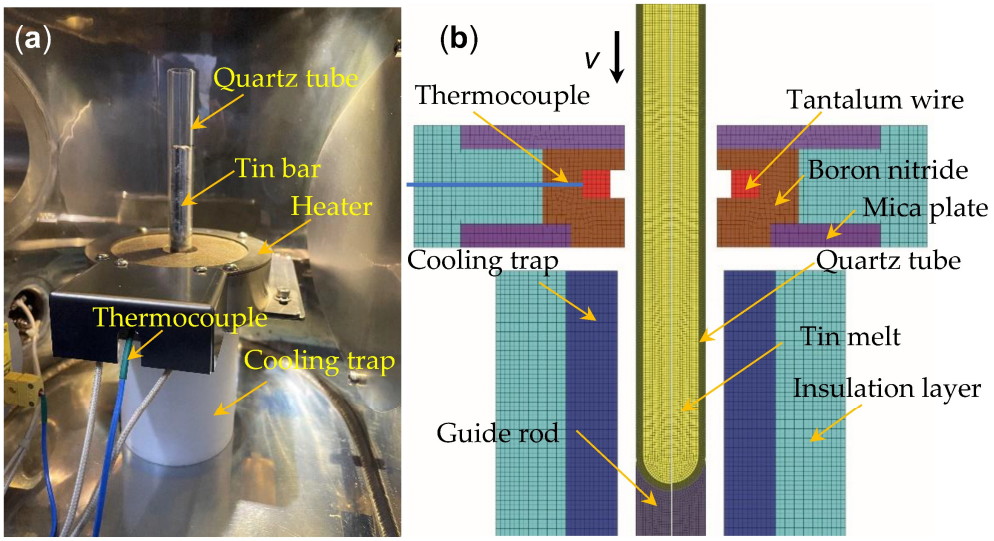

Figure 1. (**a**) Experimental setup for the vertical zone refining process. (**b**) Schematic representation of the heating and cooling unit, including the grid partitioning scheme used in the model.

In the CFD simulation of the vertical zone refining process for Sn-1 wt.%Bi, the initial pressure within the computational domain was set to 0.03 MPa, and the initial temperature to 25 °C. The initial Bi content in the Sn rod before the first zone pass was 1 wt.%, with subsequent Bi distributions based on the solute field simulation results from the preceding pass. Convective heat transfer between the inner and outer walls of the vacuum chamber was neglected, and all boundary conditions were set to no-slip. The pressure–velocity coupling algorithm was employed with a first-order upwind scheme, and the convergence criterion for equation residuals was set to 10^{-3}.

The simulations utilized the solidification–melting and component transport models in Fluent software v.17.2 [21], with the following assumptions: (1) the Boussinesq approximation was applied for thermal and solute convection; (2) the solute partition coefficient remained constant throughout the zone refining process; (3) the melt was treated as a laminar, Newtonian fluid; and (4) the Voller–Beckerman solute segregation equation [22,23] was used to model solute migration. The key control equations for the simulation are outlined below:

1. Solute Concentration in the Liquid Phase:

$$C_l = C_0[1 - (1 - \alpha' k_0) f_s]((k_0 - 1)/(1 - \alpha' k_0)) = C_s/k_0 \quad (1)$$

where C_l is the concentration of Bi in the liquid phase, C_s is the concentration of Bi in the solid phase, and C_0 is the initial concentration of the impurity element. α' is the back-diffusion coefficient, f_s is the solid phase fraction, and k_0 is the equilibrium partition coefficient.

2. Density of the Melt:

$$\rho_l = \rho_l(T, C_l) = \rho_0[1 - \beta_T(T - T_0) - \beta_c(C_l - C_0)] \quad (2)$$

where ρ_l is the density of the melt, ρ_0 is the density of the Sn-1 wt.%Bi alloy, β_T is the thermal expansion coefficient, β_c is the solute expansion coefficient, T is the temperature, and T_0 is the initial temperature.

3. Energy Equation:

$$\frac{\partial}{\partial t}(pH) + \nabla \cdot \left(\rho \vec{v} H\right) = \nabla \cdot (k \nabla T) + \nabla \cdot \left(\rho \vec{v} \Delta H\right) \quad (3)$$

$$H = h + \Delta H = \int_{T_0}^{T} C_P \mathrm{d}T + f_l \Delta H_f \quad (4)$$

where t is time, p is pressure, H is enthalpy, ρ is transient density, $\vec{v}$ is the velocity vector, k is thermal conductivity, h is sensible enthalpy, ΔH is latent heat, C_P is specific heat capacity, ΔH_f is the latent heat of melting, and f_l denotes the liquid phase fraction.

4. Momentum Equation:

$$\frac{\partial}{\partial t}\left(\rho \vec{v}\right) + \nabla \cdot \left(\rho \vec{v} \vec{v}\right) = -\nabla p + \nabla \cdot (\overline{\tau}) + \rho \vec{g} + \vec{F_b} + \vec{S} \quad (5)$$

$$\vec{S} = \frac{(1 - f_l)^2}{\left({f_l}^3 + \varepsilon\right)} A_{mush} \vec{v} \quad (6)$$

where $\overline{\tau}$ is the stress tensor, $\vec{g}$ is gravitational acceleration, $\vec{F_b}$ represents the volume force, $\vec{S}$ is the momentum source term, ε is a small value to prevent division by zero (0.001), and A_{mush} is the mushy zone constant.

5. Solute Transport Equation:

$$\frac{\partial(\rho C_l)}{\partial t} + \nabla \cdot \left(\rho[1 - f_s] \vec{v} C_l\right) = \nabla \cdot (\rho[1 - f_s] D_l \nabla C_l) - k_0 C_l \frac{\partial(\rho f_s)}{\partial t} + \frac{\partial(\rho f_s C_l)}{\partial t} - \alpha' f_s \frac{\partial(\rho C_l)}{\partial t} \quad (7)$$

where D_l is the diffusion coefficient of Bi in the liquid phase.

3. Result and Discussion

3.1. Numerical Simulation of Processing Parameters' Impact

To explore the influence of the heater temperature and pulling rate on impurity migration in tin melts during vertical zone refining, numerical simulations were conducted under four specific conditions. The first set of simulations used a constant pulling rate of 20 μm/s, with heater temperatures of 410 °C and 420 °C (SIM-410-20 and SIM-420-20, respectively). The second set involved a constant heater temperature of 415 °C, with pulling rates of 10 μm/s and 30 μm/s (SIM-415-10 and SIM-415-30, respectively), as detailed in Table 2.

Table 2. Process conditions and sample identifiers for vertical zone refining numerical simulations.

	Heater Temperature (°C)	Pulling Rate (μm/s)
SIM-410-20	410	20
SIM-420-20	420	20
SIM-415-10	415	10
SIM-415-30	415	30

Figure 2 presents the temperature distribution and solid–liquid interface morphology of the tin melt after a quartz tube withdrawal of 78 mm under these four experimental conditions. The black lines on either side in the figures indicate the heater for positional reference. The results indicate that, with a constant pulling rate of 20 μm/s, increasing the heater temperature from 410 °C to 420 °C raised the maximum temperature at the melt centerline from 243 °C to 270 °C. The contour of the liquid-phase fraction showed an increase in molten zone height from 29.8 mm to 32.6 mm, with both the upper and lower interfaces of the molten zone shifting accordingly. The upper interface remained horizontal, while the lower interface was slightly convex (Figure 2a,b). Conversely, when the heater temperature was maintained at 415 °C, increasing the pulling rate from 10 μm/s to 30 μm/s reduced the maximum temperature at the melt from 257 °C to 249 °C. The molten zone height decreased from 34.9 mm to 28.0 mm, with a noticeable drop in the upper interface and a slight rise in the lower

interface. The interface morphology remained consistent, with a horizontal upper interface and a convex lower interface (Figure 2c,d).

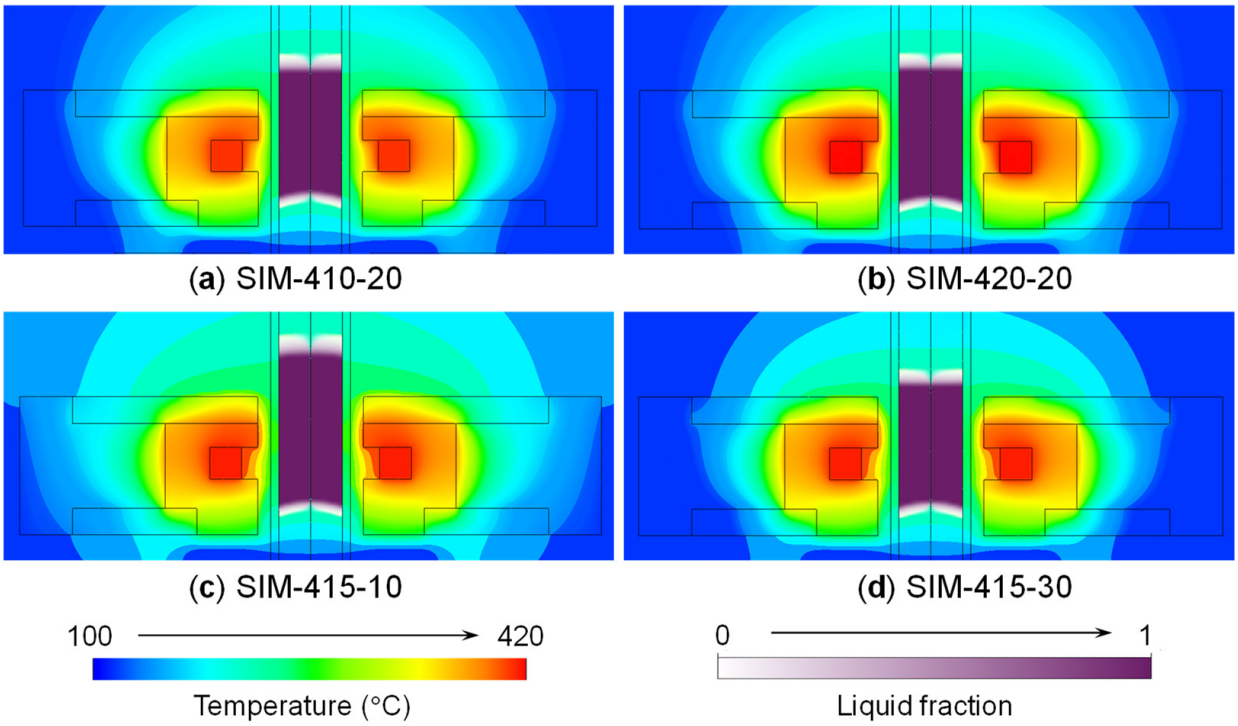

Figure 2. Numerical simulation results showing the temperature field and solid–liquid interface characteristics during downward withdrawal at the same displacement of 78 mm under four different vertical zone refining conditions.

Figure 3 further illustrates the evolution of molten zone height and interface morphology during vertical zone refining. It depicts the variations in molten zone height and the relative positions of the upper and lower solid–liquid interfaces at different withdrawal positions under the conditions of 410 °C and 20 μm/s. Throughout the zone refining process, the solid–liquid interface morphology remained relatively stable, with a flat upper interface and a slightly convex lower interface. As the quartz tube was withdrawn from 13 mm to 26 mm, the molten zone height increased rapidly from 15.5 mm to 22.9 mm. Further pulls to 52 mm, 78 mm, and 100 mm resulted in more gradual increases, reaching 27.0 mm, 29.8 mm, and 31.4 mm, respectively. Beyond 100 mm, the height decreased to 24.7 mm at 120 mm due to the absence of additional solid alloy. Despite these fluctuations, it should be noted that the slightly convex shape of the lower interface remained consistent, which favored single-crystal growth and enhanced impurity removal [24,25].

Figure 4 presents the relationship between molten zone height and withdrawal distance under four different processing conditions. As in Figure 3, molten zone height increased rapidly at first and peaked near 100 mm before declining. To ensure the accuracy and reliability of the numerical simulations, vertical zone refining experiments were conducted using 6N-grade high-purity tin under the same conditions. In the final stage, small vibrations were introduced into the experimental setup to observe the onset of surface melting in the high-purity tin within the quartz tube. By correlating this observation with the corresponding withdrawal distance, the maximum molten zone height was inferred. As depicted in Figure 4, the experimentally measured data (represented by solid circular markers) closely align with the predictions from the numerical simulations. Additionally, the numerical simulations reveal that variations in the pulling rate have a more pronounced impact on the molten zone height than changes in the heater temperature. For example, at a withdrawal distance of 96 mm with a heater temperature of 415 °C, increasing the pulling rate from 10 μm/s to 30 μm/s caused the molten zone height to decrease from 37.6 mm to 28.7 mm. In contrast, increasing the heater temperature from 410 °C to 420 °C at a constant pulling rate of 15 μm/s resulted in only a modest increase from 31.6 mm to 34.0 mm.

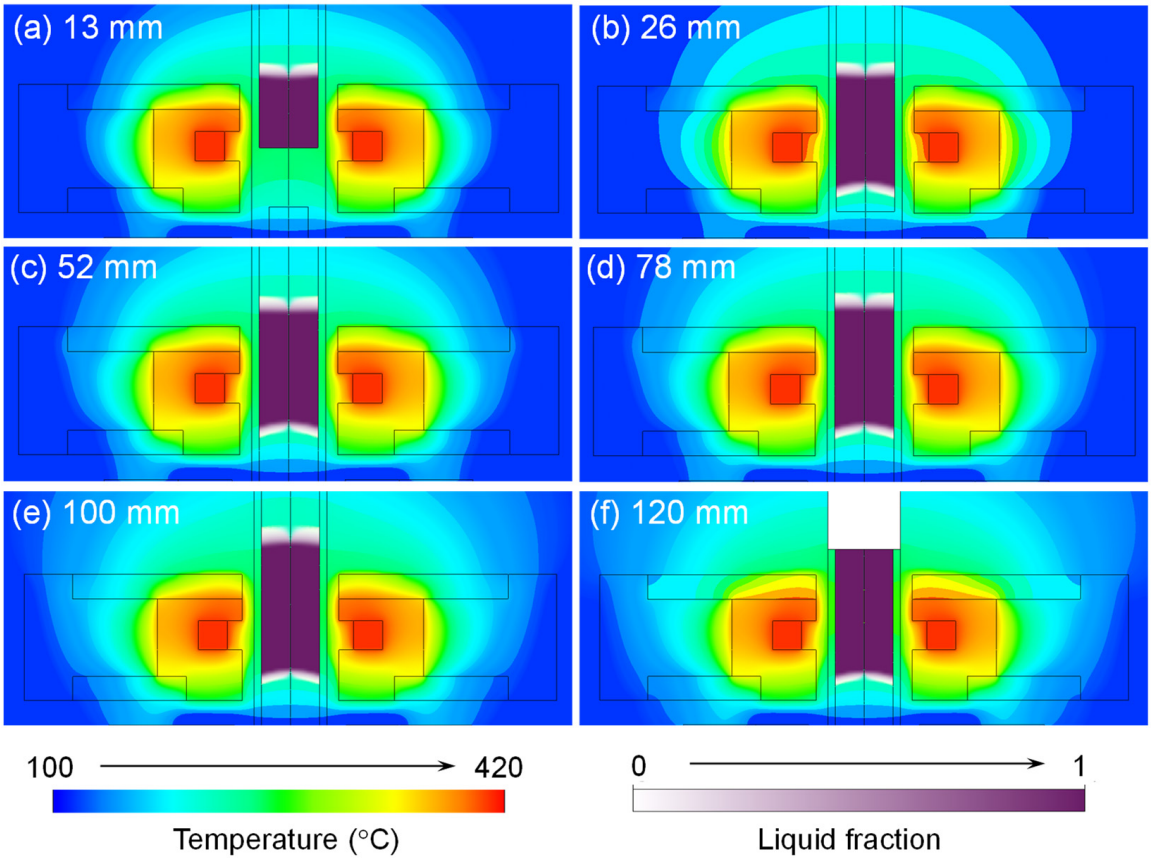

Figure 3. Numerical simulation results depicting the evolution of the solid–liquid interface at different withdrawal distances under a heater temperature of 410 °C and a pulling rate of 20 μm/s.

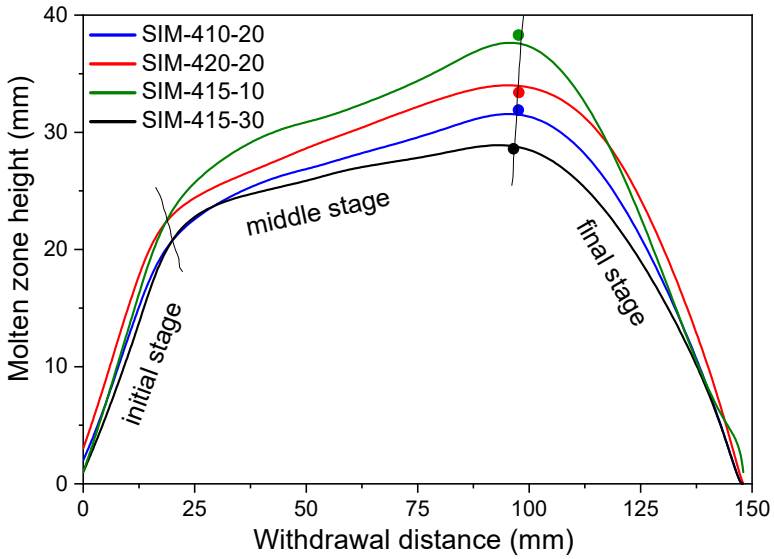

Figure 4. Relationship curves between the molten zone height as a function of the withdrawal distance under four different vertical zone refining process conditions.

Figure 5a depicts the distribution of Bi element in the central cross-section of the SIM-410-20 sample during a continuous zone refining process with nine passes, conducted at a heater temperature of 410 °C and a pulling rate of 20 μm/s. Given that the partition coefficient of Bi in the Sn melt is 0.30 (less than 1), we observed that, after the initial zone pass, impurities migrated significantly toward the upper region of the sample along the axial height. Radially, impurities accumulated along the centerline below the rod and at the edges above it. In subsequent passes, impurities continued to

concentrate along the axial centerline, with their concentrations increasing as they migrated upwards. This resulted in a progressively smaller zone of impurity accumulation.

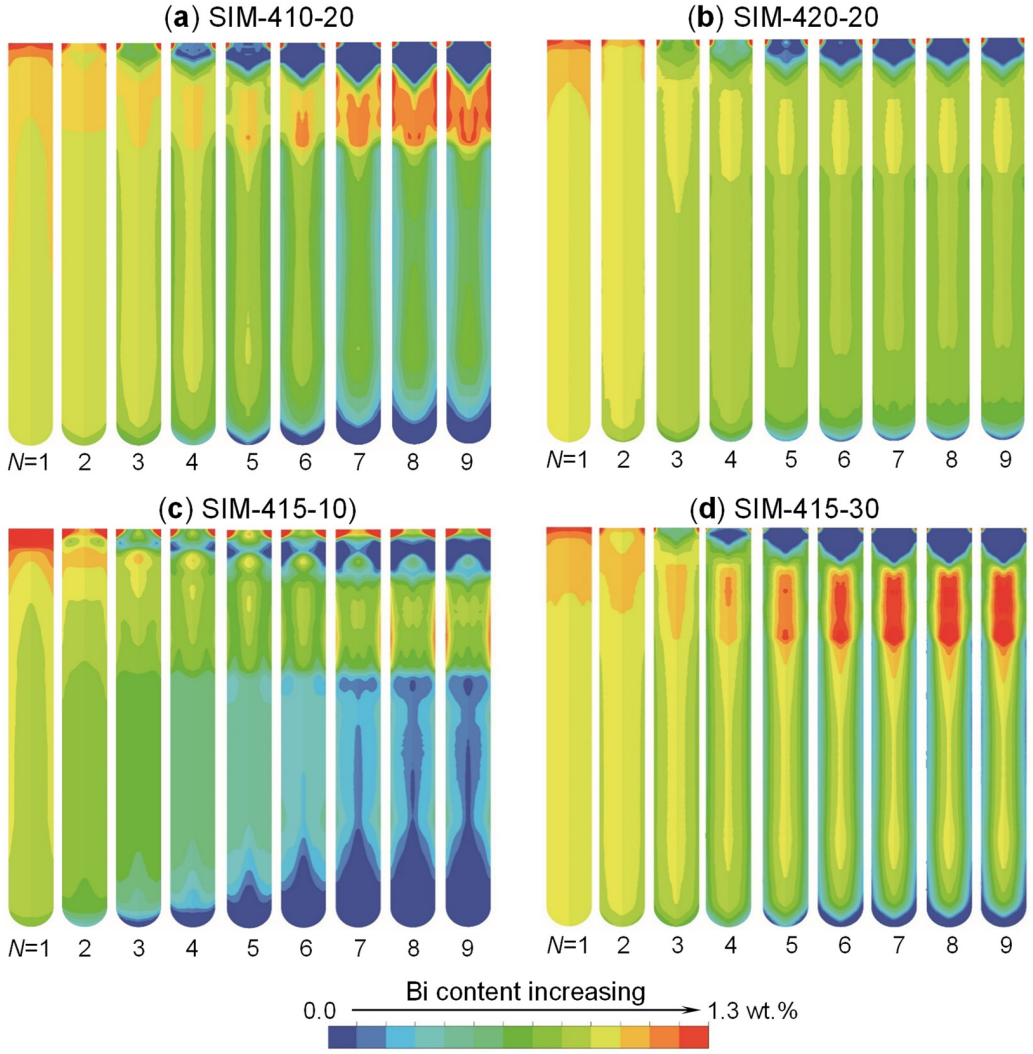

Figure 5. Bi distribution maps on the central cross-section of samples corresponding to the zone pass under different vertical zone refining conditions.

A notable rhombus-shaped impurity-free (negative segregation) zone formed at the top of the sample, expanding with each pass and leading to a concentration of impurities near the top, though not at the very peak. This behavior deviates from conventional theoretical expectations. Upon increasing the heater temperature to 420 °C while maintaining a constant pulling rate of 20 μm/s, the migration behavior and formation of the impurity-free zone at the top resembled those observed at 410 °C. However, for the SIM-420-20 sample, the impurity separation effectiveness deteriorated markedly compared to SIM-410-20. The rhombus-shaped negative segregation zone at the top clearly shrunk, and the impurity concentration characteristics became less distinct (Figure 5b).

Figure 5c illustrates the evolution of Bi element distribution in the SIM-415-10 sample during nine continuous zone passes at a heater temperature of 415 °C and a pulling rate of 10 μm/s. As with the SIM-410-20 sample, impurities migrated towards the top along the axial height. However, in this case, impurities were more concentrated at the rod edges in contact with the quartz tube, forming a gate-shaped negative segregation zone at the rod's top. The accumulation of impurities near the top of the rod was less pronounced, concentrating at the very top edge, while a substantial high-purity zone formed at the bottom. When the pulling rate was increased to 30 μm/s, the impurity distribution in the SIM-415-30 sample after nine passes became similar to that observed in SIM-420-20 and SIM-410-20, with impurities concentrated near the top along the centerline. Although

the negative segregation zone at the top remained visible, the high-purity zone at the bottom was virtually absent, indicating reduced impurity separation (Figure 5d).

To assess impurity separation effectiveness under various conditions, we defined the ratio of the average Bi content in the lower 80% of the sample height to the initial Bi content (C_{80}/C_0) as the relative impurity content. A lower ratio indicates better impurity separation. As illustrated in Figure 6a, the C_{80}/C_0 ratios for the SIM-410-20 and SIM-420-20 samples were nearly identical after five zone passes. With additional passes, the ratio for SIM-420-20 remained stable, indicating that further zone refining does not enhance impurity separation under these conditions. In contrast, the ratio for SIM-410-20 continued to decrease, reaching values of 0.405 and 0.554 after nine passes, respectively. Figure 6b demonstrates that the SIM-415-10 sample consistently outperformed the SIM-415-30 sample in terms of impurity separation, although both stabilized after seven passes. After nine passes, their C_{80}/C_0 values were 0.352 and 0.598, respectively. Practically, lower heater temperatures and slower pulling rates are more favorable for achieving better impurity separation in specific regions.

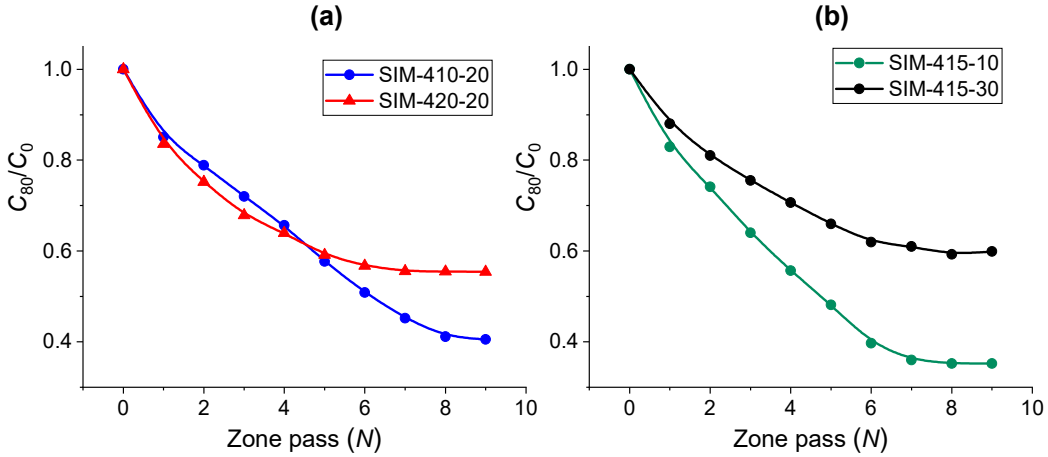

Figure 6. Correlation between the average impurity concentration ratio within the lower 80% of the rod height (C_{80}/C_0) and the number of zone passes for samples under different vertical zone refining conditions.

The migration and accumulation of impurity elements during zone refining are intricately linked to the flow dynamics of the Sn melt within the quartz tube. The spatial distribution of impurities during multi-pass zone refining is governed by the combined effects of these melt flows. Figure 7 illustrates the state of melt flow in the quartz tube at various stages of the process, corresponding to different withdrawal distances, under four distinct zone refining conditions. For the SIM-410-20 sample, at an initial withdrawal distance of 20 mm, the melt exhibited a centripetal, counterclockwise vortex. As the process advanced, solidification occurred at the lower end of the melt, while additional tin melted at the upper end. When the withdrawal distance reached 78 mm, the maximum flow velocity along the centerline reached 1.47 mm/s. This counterclockwise vortex drove impurities towards the solid–liquid interface, concentrating them in the central region. At a withdrawal distance of 110 mm, a weak clockwise vortex appeared at the top of the tin melt, as indicated by the ellipse in the figure, which was crucial for forming the negative segregation zone. As the withdrawal distance increased to 120 mm, the height of the molten zone dropped sharply; however, the remaining melt continued to sustain the counterclockwise vortex.

Similar flow patterns were observed under other conditions, although the intensity of the flow varied. For instance, at a pulling rate of 20 μm/s, increasing the heater temperature from 410 °C to 420 °C resulted in corresponding maximum central flow velocities of 1.47 mm/s and 3.03 mm/s, respectively. When the heater temperature was set to 415 °C and the pulling rate increased from 10 μm/s to 30 μm/s, the maximum flow velocities were 1.87 mm/s and 1.39 mm/s, respectively. Notably, the lower pulling rate of 10 μm/s resulted in a dual vortex pattern at a withdrawal distance of 78 mm, which may explain the formation of a gate-shaped negative segregation zone at the top of the melt rather than a rhombus-shaped negative segregation zone. These findings suggest that, while both heater temperature and pulling rate influence melt flow, temperature variations have a more pronounced effect on flow behavior compared to changes in the pulling rate.

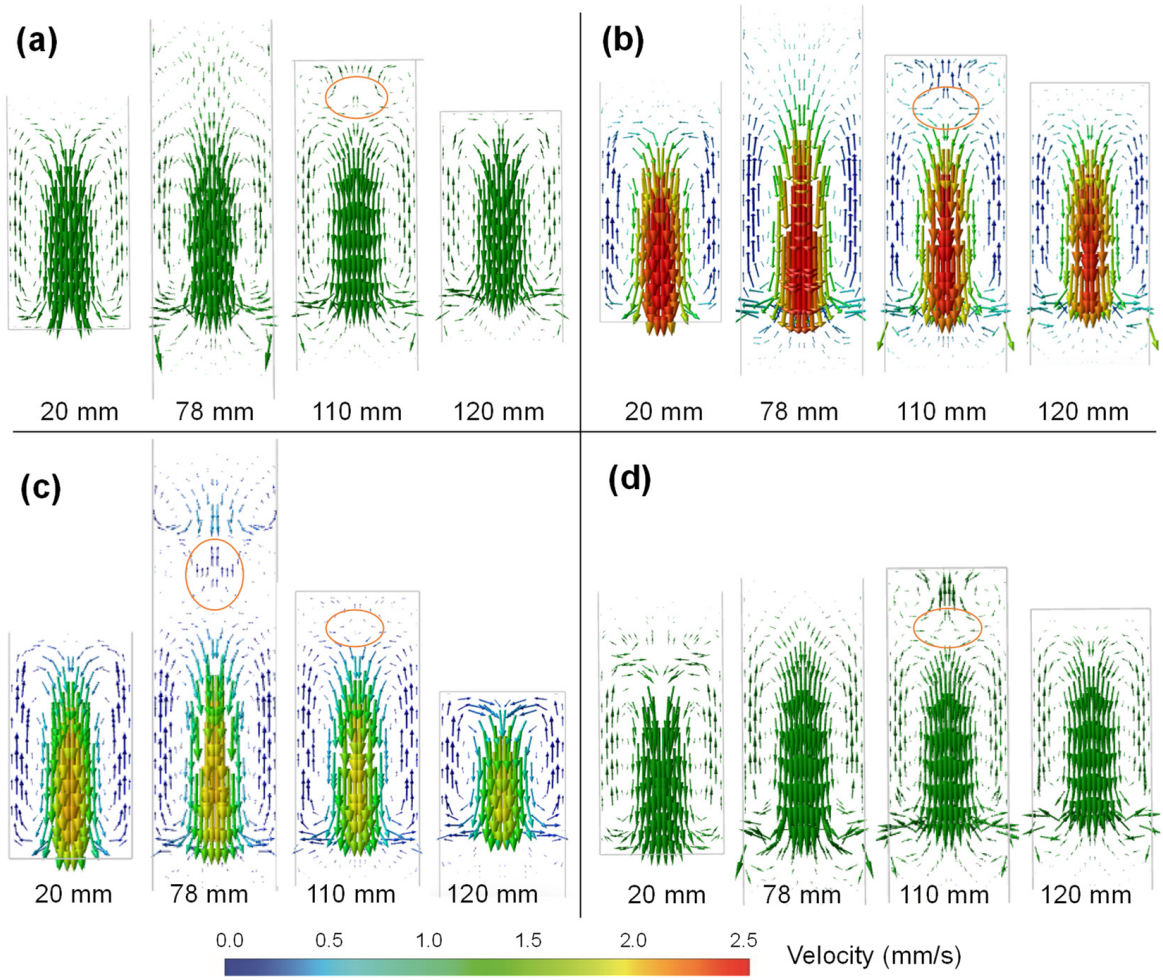

Figure 7. Vector field representations of melt flow at withdrawal distances of 20 mm, 78 mm, 110 mm, and 120 mm under four different vertical zone refining conditions: (**a**) SIM-410-20, (**b**) SIM-420-20, (**c**) SIM-415-10, and (**d**) SIM-415-30. Elliptical markers highlight the presence of a weak clockwise vortex observed at the top region of the molten tin.

Accurate prediction of impurity distribution during zone refining is essential for optimizing process parameters. As mentioned in the Section 1, Lee et al. proposed a model based on solidification theory for impurity distribution in horizontal zone refining. According to their model, impurity distribution shows a continuous rise at the rod's tail [14]. Cheung et al. introduced a genetic algorithm to determine the optimal zone length for each pass, but their model also relies on solidification theory and does not account for the effects of quartz boat walls on melt flow [15]. Our multi-physics numerical simulations reveal that in vertical zone refining, the tin rod sample can be divided into four distinct regions: a high-purity zone at the bottom, a mid-platform purity zone, a negative segregation zone near the top, and an impurity-rich zone at the top. These simulations consider impurity back-diffusion in the solid phase and melt flow at various withdrawal distances. Notably, the appearance of a negative segregation zone in vertical zone refining contrasts with conventional understanding from horizontal zone refining due to the reverse vortex created by the solid interface at the end of the molten zone.

3.2. Vertical Zone Refining Experiments for 7N-Grade Ultra-High-Purity Tin

Based on the numerical simulation results, 6N-grade tin with an initial total impurity content of 0.264 ppm was selected for vertical zone refining experiments. These experiments were conducted using nine passes under three distinct conditions: heater temperatures of 410 °C and 405 °C, combined with pulling rates of 10 μm/s and 5 μm/s. The samples produced under these conditions were designated as VZR-410-10, VZR-405-10, and VZR-405-5, respectively (see Table 3).

Table 3. Process conditions and sample identifiers for vertical zone refining experiments.

	Heater Temperature (°C)	Pulling Rate (μm/s)
VZR-410-10	410	10
VZR-405-10	405	10
VZR-405-5	405	5

After completing nine passes, samples were collected from the bottom, middle, and top regions of the zone-refined rods and analyzed using GDMS to measure the concentrations of 15 major impurity elements. The impurity content results for the raw 6N-grade tin and various regions of the zone-refined samples are summarized in Table 4. The analysis revealed that after nine passes, five impurities—Zn, Ca, Mg, Au, and In—were below the detection limits of the GDMS equipment across all test regions. Additionally, Ag and Pb were below the detection limits in the bottom and middle regions of all samples, although small amounts of Ag and Pb were detected in the top regions, suggesting that the k_{eff} values of these elements in the tin melt are likely less than 1.

Table 4. GDMS results for 6N-grade Sn starting material and three zone-refined samples (unit: ppm).

6N-Grade Sn Starting Material		VZR-410-10			VZR-405-10			VZR-405-5		
		Bottom	Middle	Top	Bottom	Middle	Top	Bottom	Middle	Top
Co	0.001	—	0.001	0.002	—	—	0.003	—	0.002	0.005
Zn	—	—	—	—	—	—	—	—	—	—
Ag	0.001	—	—	0.002	—	—	0.003	—	—	0.02
Cu	0.01	0.002	0.009	0.06	0.002	0.003	0.04	—	—	0.63
Ca	—	—	—	—	—	—	—	—	—	—
Al	0.005	—	—	0.006	—	0.002	0.007	0.002	0.001	0.006
Mg	—	—	—	—	—	—	—	—	—	—
Ni	0.007	0.001	0.006	0.004	—	0.002	0.01	—	—	0.34
Pb	0.005	—	—	0.004	—	—	0.008	—	—	0.01
Au	—	—	—	—	—	—	—	—	—	—
Fe	0.13	0.06	0.12	0.97	0.02	0.06	0.98	—	0.01	2.6
In	—	—	—	—	—	—	—	—	—	—
Bi	0.005	0.003	0.01	0.02	0.002	0.005	0.02	0.003	0.003	0.03
Sb	0.08	0.09	0.08	0.05	0.11	0.09	0.06	0.08	0.08	0.08
As	0.02	0.02	0.02	0.03	0.02	0.02	0.04	0.02	0.01	0.05
Total	0.264	0.176	0.246	1.146	0.154	0.182	1.171	0.105	0.106	3.771

The addition of — indicates the content below the GDMS detection limit of the impurity element.

Figure 8 illustrates the distribution of the remaining eight impurity elements and the total impurity content along the height of the zone-refined rods. Elements such as Co, Al, Bi, Cu, Fe, and Ni showed a strong tendency to accumulate at the top, indicating that their k_{eff} values were significantly less than 1. For example, Bi demonstrated a notable separation ratio in the bottom region, with impurity levels ranging from 40% to 60% after nine zone passes, aligning well with the predicted Bi removal range shown in Figure 6. In the middle region, moderate segregation was observed, while substantial accumulation occurred at the top. In contrast, the As content in the bottom and middle regions remained relatively unchanged from its initial value (0.02 ppm), with levels of 0.03 ppm, 0.02 ppm, and 0.05 ppm detected in the top region, indicating a slight migration towards the top. This suggests that the k_{eff} for As was slightly less than 1, but very close to it. This result differs somewhat from the previous study [18], where a more pronounced decrease in As content was observed in the bottom and middle regions. This discrepancy implies that as the initial tin purity increases, separating As becomes progressively more difficult. For Sb, the contents in the bottom regions of the VZR-410-10 and VZR-405-10 samples were 0.09 ppm and 0.11 ppm, respectively, higher than the initial value (0.08 ppm), with minor reductions in the middle and top regions. This suggests a higher concentration at the bottom and lower concentrations at the top, indicating that the k_{eff} for Sb is greater than 1. However, in the VZR-405-5 sample, no significant change in Sb content was observed across all regions (0.08 ppm).

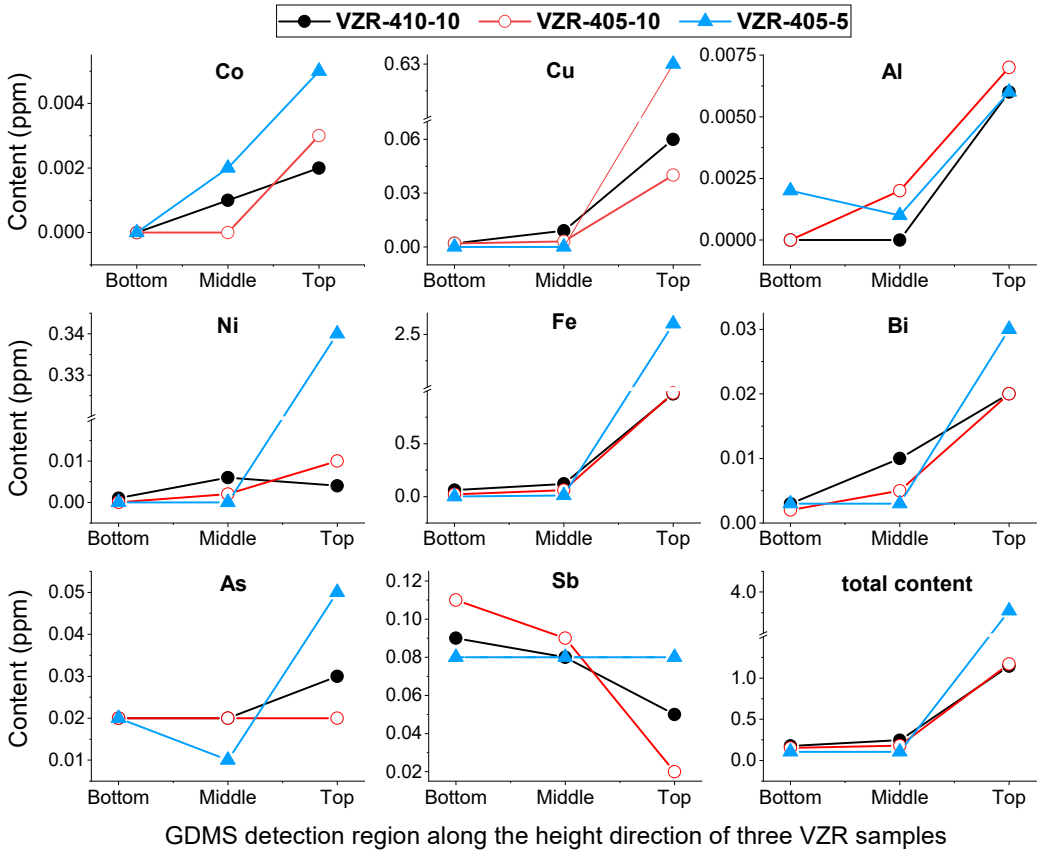

Figure 8. Spatial profiles of impurity elemental concentrations and total content along the rod height under three vertical zone refining conditions.

In a related study, Zhang et al. conducted horizontal zone refining experiments using 4N-grade tin (99.99682 wt.%). Their results showed that the k_{eff} values for elements such as Ag, Al, As, Bi, Ca, Cu, Fe, Ni, Pb, Au, Co, and Zn were all less than 1, while the k_{eff} for Sb was greater than 1. They noted that reducing the moving rate from 1.4 mm/min to 0.6 mm/min improved the purity of the middle section of the ingot from 99.99824 wt.% to 99.99906 wt.% after ten passes [13]. Similarly, in a previous study involving 5N-grade tin (99.99983 wt.%), substantial reductions in impurity content were observed after nine passes at 405 °C and a pulling rate of 10 μm/s, resulting in tin purity exceeding 99.99994 wt.% [18]. In the present experiments with 6N-grade tin, after nine passes at 410 °C and a pulling rate of 10 μm/s, the total impurity content in the VZR-410-10 sample's bottom and middle regions decreased to 0.176 ppm and 0.246 ppm, respectively. Lowering the heater temperature to 405 °C while maintaining a pulling rate of 10 μm/s resulted in a significant reduction in impurity content for the VZR-405-10 sample, with values of 0.154 ppm and 0.182 ppm in the bottom and middle regions, respectively, yielding separation ratios of 42% and 31%. Further lowering the pulling rate to 5 μm/s for the VZR-405-5 sample reduced impurity levels to 0.105 ppm and 0.106 ppm in the bottom and middle regions, with a separation ratio exceeding 60%, resulting in a tin purity approaching 6N9. These findings confirm that vertical zone refining remains effective for producing ultra-high-purity tin, although it requires slower pulling rates and lower heating temperatures.

4. Conclusions

This study investigated the vertical zone refining process for producing ultra-high-purity tin, yielding the following key findings:

1. CFD simulations revealed that the molten zone exhibited a dynamic profile characterized by three phases: an initial rapid ascent, a slower increase, and a sharp final descent. The upper interface remained flat, while the lower interface was slightly convex. After nine passes, impurities concentrated at the top, forming a rhombus- or gate-shaped negative segregation zone. Increasing the heater temperature from 410 °C to 420 °C at a constant pulling rate of 20 μm/s reduced the Bi segregation ratio from 59.5% to 44.6%. Similarly, increasing the pulling rate from 10 μm/s to 30 μm/s at a fixed temperature of 415 °C decreased the segregation ratio from 64.8% to 40.2%.

2. Experiments using 6N-grade tin as the starting material demonstrated that the k_{eff} values for impurities such as Ag, Pb, Co, Al, Bi, Cu, Fe, and Ni were all less than 1, while the k_{eff} for As was below but very close to 1. The k_{eff} for Sb was greater than 1. Under optimal conditions (405 °C heater temperature and a pulling rate of 5 μm/s), the total impurity content decreased from 0.264 ppm to 0.105 ppm in the bottom region and to 0.106 ppm in the middle region. This yielded an impurity removal rate exceeding 60%, nearly achieving 6N9-grade purity.

In conclusion, this study underscores the potential of vertical zone refining for producing 7N-grade ultra-high-purity tin. However, additional purification steps may be necessary to remove challenging impurities, particularly As and Sb.

Author Contributions: Conceptualization, Y.Y. and H.Z.; data curation, Y.Y. and J.W.; formal analysis, Y.Y., J.W., Q.H., M.W., L.C., Y.B. and H.Z.; investigation, Y.Y., J.W., Q.H., L.C. and H.Z.; methodology, Y.Y. and H.Z.; resources, M.W. and L.C.; validation, Y.Y., Q.H., M.W., L.C., Y.B. and H.Z.; writing—original draft, Y.Y., M.W. and Y.B.; writing—review and editing, H.Z. All authors have read and agreed to the published version of the manuscript.

Funding: This work was supported by the National Natural Science Foundation of China (52074180), and the Joint Special Project on Basic and Applied Basic Research of Yunnan Tin Group (Holding) Company Limited (202301BC07001-016).

Data Availability Statement: The original contributions presented in the study are included in the article. Further inquiries can be directed to the corresponding authors.

Conflicts of Interest: Authors Qi He, Meizhen Wu, Lishi Chen and Yuxu Bao were employed by the company Yunnan Tin New Material Company Limited. The remaining authors declare that the research was conducted in the absence of any commercial or financial relationships that could be construed as a potential conflict of interest.

References

1. Versolato, O.O. Physics of laser-driven tin plasma sources of EUV radiation for nanolithography. *Plasma Sources Sci. Technol.* **2019**, *28*, 083001. [CrossRef]
2. Flosdorf, E.W.; Palmer, A.E. Purification of materials by vacuum distillation. *J. Rheol.* **1932**, *3*, 205. [CrossRef]
3. Price, J. Removal of impurities from tin by vacuum distillation. *Nature* **1952**, *169*, 792. [CrossRef]
4. Jia, G.B.; Yang, B.; Liu, D.C. Deeply removing lead from Pb-Sn alloy with vacuum distillation. *Trans. Nonferr. Metal. Soc.* **2013**, *23*, 1822–1831. [CrossRef]
5. Nan, C.B.; Yang, H.W.; Yang, B.; Liu, D.C.; Xiong, H. Experimental and modeling vapor-liquid equilibria: Separation of Bi from Sn by vacuum distillation. *Vacuum* **2017**, *135*, 109–114. [CrossRef]
6. Pu, Z.H.; Han, J.B.; Li, Y.F.; Dai, Y.N.; Yang, B.; Wang, A.X. Removal of arsenic from crude tin by vacuum distillation. *Mater. Trans.* **2018**, *59*, 311–315. [CrossRef]
7. You, Y.J.; Pu, Z.H.; Li, Y.F.; Yang, B.; Xu, J.J. Study on separation of Sn-Sb alloy by vacuum distillation. In *10th International Symposium on High-Temperature Metallurgical Processing, The Minerals, Metals & Materials Series*; Springer: Cham, Switzerland, 2019; pp. 361–370.
8. Filzwieser, A.; Filzwieser, I.; Konetschnik, S. New technology for electrorefining of copper. *JOM* **2012**, *64*, 1290–1295. [CrossRef]
9. Gana, R.E.; Figueroa, M.G.; Kattan, L.; Orpinas, J.M. The anode-support system: An alternative for the electrorefining of tin in sulphuric acid medium. *J. Appl. Electrochem.* **1993**, *23*, 60–65. [CrossRef]
10. Kulcsar, T.; Toth, G.B.; Kekesi, T. Complex evaluation and development of electrolytic tin refining in acidic chloride media for processing tin-based scrap from lead-free soldering. *Miner. Process. Extr. Metall.* **2016**, *125*, 228–237. [CrossRef]
11. Rimaszeki, G.; Kulcsar, T.; Kekesi, T. Investigation and optimization of tin electrorefining in hydrochloric acid solutions. *J. Appl. Electrochem.* **2012**, *42*, 573–584. [CrossRef]
12. Zhang, X.X.; Friedrich, S.; Friedrich, B. Production of high purity metals: A review on zone refining process. *J. Cryst. Process Technol.* **2018**, *8*, 33–55. [CrossRef]
13. Zhang, H.; Zhao, J.Y.; Xu, J.J.; Li, Y.F.; Pu, Z.H.; Xu, B.Q.; Yang, B. Preparation of high-purity tin by zone melting. *Russ. J. Non-Ferr. Met.* **2020**, *61*, 9–20. [CrossRef]
14. Lee, H.Y.; Oh, J.K.; Lee, D.H. Purification of tin by zone refining with development of a new model. *Metall. Trans. B* **1990**, *21*, 455–461. [CrossRef]
15. Cheung, T.; Cheung, N.; Tobar, C.M.T.; Mei, P.R.; Garcia, A. Zone refining of tin: Optimization of zone length by a genetic algorithm. *Mater. Manuf. Process.* **2013**, *28*, 746–752. [CrossRef]
16. Shang, Z.W.; Lian, Z.H.; Li, M.J.; Han, K.; Zheng, H.X. Machine-learning-assisted multi-objective optimization in vertical zone refining of ultra-high purity indium. *Sep. Purif. Technol.* **2023**, *305*, 122430. [CrossRef]

17. Li, M.X.; Tian, Q.L.; Wu, M.Z.; Peng, J.B.; Zhang, J.T.; Chen, L.S.; Lu, X.W.; Xu, Z.S.; Zheng, H.X. Numerical simulation analysis on solute redistribution of In–1 wt%Sn alloy during multipass vertical zone refining process. *J. Cryst. Growth* **2021**, *565*, 126156. [CrossRef]
18. Wen, J.J.; Wu, M.Z.; Peng, J.B.; Zheng, H.X. Purification of high-purity tin via vertical zone refining. *Separations* **2023**, *10*, 380. [CrossRef]
19. Massalski, T.; Murray, J.; Bennett, L.; Baker, H. *Binary Alloy Phase Diagrams*; American Society for Metals: Detroit, MI, USA, 1986; Volume 3, p. 2874.
20. Hoshino, Y.; Utsunomiya, T. Purification of tin by a new method of zone refining. *Sep. Sci. Technol.* **1980**, *15*, 1521–1531. [CrossRef]
21. Jeong, C.H.; Kang, K.; Park, U.J.; Lee, H.J.; Kim, H.S.; Park, J.Y.; Lee, S.H. Numerical investigation on the evolution of thin liquid layer and dynamic behavior of an electro-thermal drilling probe during close-contact heat transfer. *Appl. Sci.* **2021**, *11*, 3443. [CrossRef]
22. Voller, V.R.; Beckerman, C. Approximate models of microsegregation with coarsening. *Metall. Mater. Trans. A* **1999**, *30*, 3016. [CrossRef]
23. Voller, V.R. On a general back-diffusion parameter. *J. Cryst. Growth* **2001**, *226*, 562–568. [CrossRef]
24. Hayakawa, Y.; Saitou, Y.; Sugimoto, Y.; Kumagawa, M. Analysis of impurity concentration distributions in pulled semiconductor crystals. *J. Electron. Mater.* **1990**, *19*, 145–149. [CrossRef]
25. Watauchi, S.; Tanaka, I.; Hayashi, K.; Hirano, M.; Hosono, H. Crystal growth of $Ca_{12}Al_{14}O_{33}$ by the floating zone method. *J. Cryst. Growth* **2002**, *237*, 801–805. [CrossRef]